

Hydrodynamic forces involving deformable interfaces at nanometer separations

Rogério Manica,^{1,2} Jason N. Connor,^{3,4} Raymond R. Dagastine,¹ Steven L. Carnie,¹ Roger G. Horn,⁴ and Derek Y. C. Chan^{1,2,5,a)}

¹Particulate Fluids Processing Centre, The University of Melbourne, Parkville, Victoria 3010, Australia

²Institute of High Performance Computing, Singapore 117528

³PELM Centre, Central Queensland University, Gladstone, Queensland 4680, Australia

⁴Ian Wark Research Institute, University of South Australia, Mawson Lakes, SA 5095, Australia

⁵Department of Mathematics, National University of Singapore, Singapore 117543

(Received 4 June 2007; accepted 11 January 2008; published online 5 March 2008)

A model is developed to describe the dynamic forces acting between two deformable drops, or between one drop and a solid surface, when they are in relative axisymmetric motion at separations of $\lesssim 100$ nm in a Newtonian liquid. Forces arise from hydrodynamic pressure in the draining liquid film that separates the interfaces and from disjoining pressure due to repulsive or attractive surface forces. Predictions of the model are successfully compared with recent experimental measurements of the force between two micrometer-scale surfactant stabilized decane drops in water in an atomic force microscope [S. L. Carnie, D. Y. C. Chan, C. Lewis, R. Manica, and R. R. Dagastine, *Langmuir* **21**, 2912 (2005); R. R. Dagastine, R. Manica, S. L. Carnie, D. Y. C. Chan, G. W. Stevens, and F. Grieser, *Science* **313**, 210 (2006)] and with subnanometer resolution measurements of time-dependent deformations of a millimeter-scale mercury drop approaching a flat mica surface in a modified surface force apparatus [J. N. Connor and R. G. Horn, *Faraday Discuss.* **123**, 193 (2003); R. G. Horn, M. Asadullah, and J. N. Connor, *Langmuir* **22**, 2610 (2006)]. Special limits of the model applicable to small and moderate deformation regimes are also studied to elucidate the key physical ingredients that contribute to the characteristic behavior of dynamic collisions involving fluid interfaces. © 2008 American Institute of Physics. [DOI: [10.1063/1.2839577](https://doi.org/10.1063/1.2839577)]

I. INTRODUCTION

In many multiphase processes ranging from ore flotation in the mineral industry to controlling emulsion stability in the manufacture of pharmaceutical and health care products, an important objective is to quantify and control the interaction involving deformable interfaces. For instance, the stability of two interacting drops in a suspension depends on the interplay between the intrinsic electrochemical forces between the interfaces of the drops and forces arising from the hydrodynamic flow in the thin (~ 1 – 100 nm) film between the drop surfaces. Deformations of the drop surfaces also play a key role in modulating these interaction mechanisms.

There have been a number of adaptations of the atomic force microscope (AFM) to measure both static forces involving deformable bubbles^{1–4} and oil drops^{5–14} in solution and the dynamic forces that arise when the drops in such systems are in relative motion.^{15–17} In AFM measurements of dynamic forces between two oil drops in water, the drops are mounted on the AFM cantilever and on the substrate which are then driven together and separated according to a preset velocity schedule. The resulting time and separation dependent force that arise from hydrodynamic flow of the aqueous thin film between the deformable drops as well as electrical double layer interactions is measured by monitoring the deflection of the cantilever (Fig. 1). In typical force measure-

ments between decane emulsion drops of radii in the range 40 – 500 μm stabilized by anionic surfactants (sodium dodecyl sulfate) the dynamic forces as a function of displacement can be measured with a precision within 0.1 nN over a range of attractive and repulsive forces that span over 10 nN.^{18,19} These experiments are relevant to the study of emulsion stability because the range of relative velocities that can be achieved in the AFM experiments span the average thermal velocity of emulsion drops in the same size range in solution. While AFM experiments provide direct information about variations of the force between interacting deformable drops in equilibrium or in relative motion, there is at present no direct information about details of surface deformations that occur as a result of the drop-drop interaction.

In contrast, the surface force apparatus (SFA) has recently been adapted to visualize deformations of a mercury/electrolyte interface that arise from interactions with an approaching mica plate (Fig. 2). This technique provides real time measurements of the hydrodynamic drainage process of the intervening aqueous film for thicknesses down to ~ 50 nm with subnanometer resolution,^{20,21} but currently does not yield direct information about the forces or pressure distributions that give rise to the observed interfacial deformations. However, if the colloidal forces in the SFA experiments can be quantified, it is possible to extract the time-dependent hydrodynamic pressure distribution in the draining film.²² Being a conducting liquid, a bias voltage can be applied between the mercury and the bulk electrolyte to

^{a)} Author to whom correspondence should be addressed. Electronic mail: D.Chan@unimelb.edu.au.

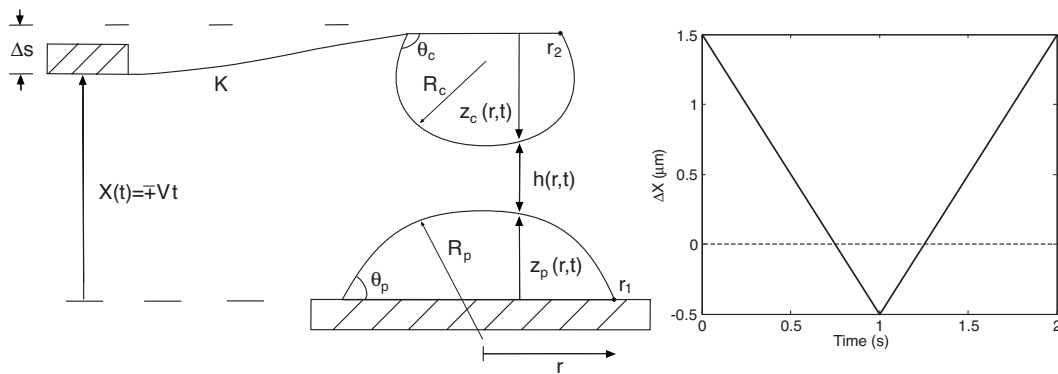


FIG. 1. Schematic configuration of the atomic force microscope (AFM) for measuring dynamic forces between two decane drops stabilized by sodium dodecyl sulfate in aqueous electrolyte solution. Relative motion between the drops is generated by specifying the displacement $X(t)$ as a function of time which can, for example, be driven at a set ramp speed V (see inset). The force is deduced from the measured cantilever deflection Δs using the independently determined spring constant K of the cantilever.

control the surface potential and hence the electrical double layer interaction that provides a disjoining pressure between the mercury and the mica plate. Strongly repulsive, strongly attractive or intermediate forms of the disjoining pressure can be obtained by selecting different values for the bias voltage (Fig. 2).

The complementary nature of the AFM and SFA experiments has been bridged by a model which has proved very successful in predicting AFM dynamic force measurements between two moving decane drops stabilized by sodium dodecyl sulfate in an aqueous electrolyte as depicted schematically in Fig. 1.^{18,19,23} The same model can also account for the time-dependent interfacial deformations of a mercury/

aqueous electrolyte interface that arise from hydrodynamic interactions with an approaching flat mica surface in the SFA (see Fig. 2).^{24,25} The theory performs equally well for interacting decane drops of 40–500 μm radius in the AFM experiments and for mercury interfaces of ~ 2 mm radius in the SFA experiments where in addition, the surface forces between the mica plate and the mercury drop arising from electrical double layer interactions can be made to be repulsive or attractive by adjusting the bias voltage between the mercury and the bulk electrolyte solution.²⁴

Given the progress thus far in direct measurements and quantitative modeling of surface deformations and dynamic force involving drops, we now aim:

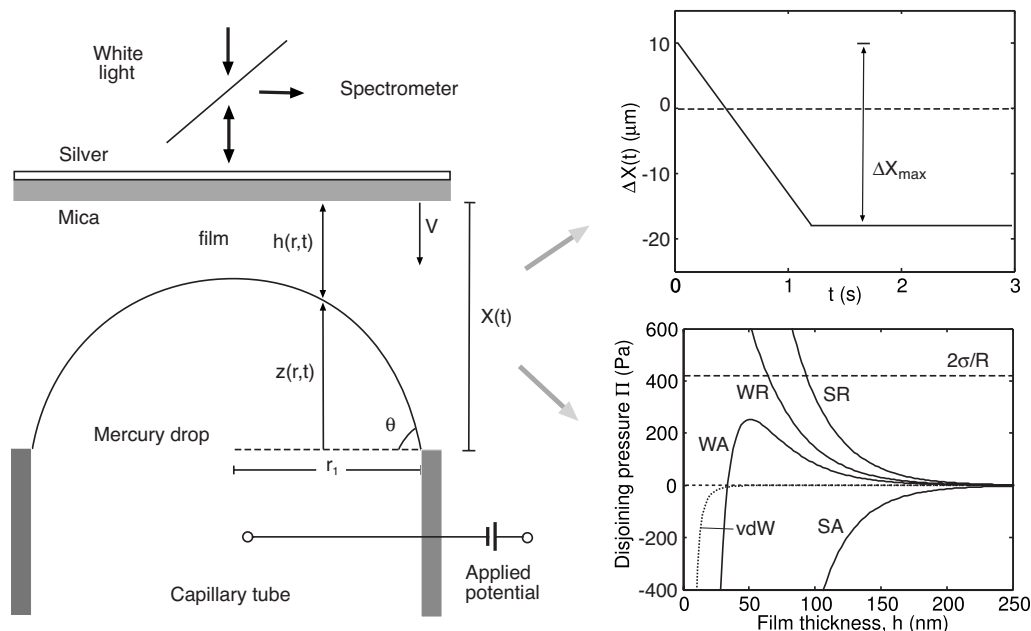


FIG. 2. Schematic diagram of a mica surface approaching a protuberant mercury drop from a sealed constant volume capillary tube of diameter ~ 2 mm. Variations of the aqueous film thickness, $h(r,t)$ resolved to subnanometer precision are obtained from analysis of fringes of equal chromatic order captured on the spectrometer. (Top inset) Variations of the position of the mica when driven at constant velocity for a fixed time. (Bottom inset) Disjoining pressures between the mica plate and the mercury drop with various surface potentials as calculated from the nonlinear Poisson–Boltzmann theory (Ref. 26); strongly repulsive (SR, -492 mV), weakly repulsive (WR, -52 mV), weakly attractive (WA, -12 mV), and strongly attractive (SA, $+408$ mV) due to electrical double layer interactions with the mica surface (-100 mV) at 0.1 mM 1:1 electrolyte concentration. It has been shown in Ref. 20 that the experimental disjoining pressure is accurately described by this theory. The disjoining pressure due to van der Waals forces is shown in the dotted line and the magnitude of the Laplace pressure ($2\sigma/R$) is indicated by the horizontal dashed line.

- (1) to elucidate the key physical principles underlying force measurements involving deformable surfaces by deriving from the general governing equations limiting forms which are valid for small and large (in the context of surface force measurements) forces;
- (2) to point out the need to use the correct far field boundary condition for the interfacial velocity that reflects the constant volume constraints of interacting drops;
- (3) to demonstrate how drive-and-stop displacement protocol of SFA measurement gives rise to constant force condition;
- (4) to undertake further comparisons between components of the dynamic force derived from SFA experiments with theory; and
- (5) to explore variations of the measured force in AFM experiments with capillary number and contact angle which can inform the design of further AFM experiments.

This paper is organized as follows: In the next section we detail the governing equations and the far field boundary condition that follows from the constant volume constraint appropriate for describing dynamic force measurements between two drops with the AFM and deformation studies using the SFA. From the displacement protocol of the SFA experiments, we make the connection between the present model and existing constant velocity²⁷ and constant force²⁸ boundary conditions. We also derive simple expressions for the force-displacement result that are valid for small and for large forces. These results are validated by comparison with the full numerical solutions of the governing equations. They prove to be accurate and convenient approximations in limiting cases that can circumvent the need for more cumbersome numerical computations. Comparisons between AFM and SFA experimental results and theory are given Sec. III. The paper closes with a discussion that considers reasons why the no-slip or immobile hydrodynamic boundary condition at the liquid/liquid interface provides the best agreement between experiments and theory and other assumptions of the model.

II. MODEL

A. Governing equations

In both the AFM and SFA experiments, the film thickness, h , the radial dimension of the film, r_f , and the unperturbed radius of curvature of the drops, R_d obey the inequalities $R_d \gg r_f \gg h$, and characteristic fluid velocities are in the regime where the familiar Stokes–Reynolds thin film drainage model applies. For a film with axial symmetry the governing equation for the film thickness $h(r, t)$ is

$$\frac{\partial h}{\partial t} = \frac{1}{12\mu r} \frac{\partial}{\partial r} \left(r h^3 \frac{\partial p}{\partial r} \right), \quad (1)$$

where μ is the shear viscosity of the aqueous film and $p(r, t)$ is the hydrodynamic pressure in the film relative to the bulk pressure. Implicit in Eq. (1) is the assumption of the no-slip hydrodynamic boundary condition at all interfaces. Theoretical predictions with the no-slip boundary condition offer the

best agreement between experiment and theory in our studies involving deformable surfaces using the AFM¹⁹ and using the SFA.²⁴ For the AFM experiments, the presence of charged surfactants (sodium dodecyl sulfate) near the critical micelle concentration renders the oil/water interface immobile. Electrokinetic mobility experiments²⁹ indicate that such emulsion drops behave hydrodynamically like a solid particle with a no-slip hydrodynamic boundary condition. For the SFA experiments with mercury drops, previous works^{30–32} indicate that since the mercury/electrolyte interface is charged, the constraint of electroneutrality of a thin electrical double layer at the charged interface gives rise to an effective no-slip hydrodynamic boundary condition.

In the configuration of a mercury drop against a rigid surface with local radius of curvature R_s , the axisymmetric deformation of the drop, consistent with the thin film approximation, is governed by the modified Young–Laplace equation in the form^{33–35}

$$\frac{\sigma}{r} \frac{\partial}{\partial r} \left(r \frac{\partial h}{\partial r} \right) = 2\sigma \left(\frac{1}{R} + \frac{1}{R_s} \right) - (p + \Pi) \quad \text{one drop (SFA)}, \quad (2a)$$

where $\Pi(h(r, t))$ is the disjoining pressure in the film due to surface forces such as electrical double layer interactions or van der Waals forces, σ is the interfacial tension of the drop and $(2\sigma/R)$ is the Laplace pressure of the drop. The SFA configuration of a rigid mica plate (Fig. 2) corresponds to the limit $R_s \rightarrow \infty$. For the AFM configuration of two interacting drops (Fig. 1) the modified Young–Laplace equation is

$$\frac{\sigma}{2r} \frac{\partial}{\partial r} \left(r \frac{\partial h}{\partial r} \right) = \frac{2\sigma}{R} - (p + \Pi) \quad \text{two drops (AFM)}, \quad (2b)$$

where $\sigma^{-1} = (\sigma_c^{-1} + \sigma_p^{-1})/2$ and $R^{-1} = (R_c^{-1} + R_p^{-1})/2$ are defined in terms of the interfacial tensions and Laplace pressures $(2\sigma_c/R_c)$ and $(2\sigma_p/R_p)$ of the two drops which may have dissimilar properties. Implicit in Eq. (2) is the assumption that deformations take place under quasiequilibrium conditions under a dynamic pressure $(p + \Pi)$.¹⁸

The instantaneous force, $F(t)$ exerted on the drop has contributions from hydrodynamics and disjoining pressures

$$F(t) \equiv 2\pi\sigma G(t) = 2\pi \int_0^\infty [p(r, t) + \Pi(h(r, t))] r dr. \quad (3)$$

This assumes that the drop radius is much larger than the range of hydrodynamic forces so that the interacting interfaces are nearly flat and parallel. The length $G(t)$ defined in Eq. (3) arises naturally in later discussions. Equations (1) and (2) are to be solved numerically in a suitable radial domain $0 < r < r_{\max}$ where the surfaces at $r > r_{\max}$ are sufficiently far apart that effects of disjoining pressure can be omitted. The initial film thickness is taken to be

$$h(r, t_{\text{start}}) = \begin{cases} h_{\text{start}} + \frac{r^2}{2R_0}, & \text{one drop (SFA),} \\ h_{\text{start}} + \frac{r^2}{R_0}, & \text{two drops (AFM),} \end{cases} \quad (4)$$

where in the one drop case $R_0^{-1} = (R_d^{-1} + R_s^{-1})$ with R_d as the unperturbed radius of the drop. For the AFM configuration of two interacting drops (Fig. 1) R_0 is the value of R in Eq. (2b) expressed in terms of the unperturbed radii of the drops. These expressions for the initial film thickness assume that the interfaces are far apart and the surfaces are undeformed.

Symmetry considerations require $\partial h / \partial r = 0$ and $\partial p / \partial r = 0$ at $r = 0$. At the outer boundary $r \sim r_{\text{max}}$, the expected asymptotic form of the pressure $p \sim r^{-4}$,²⁸ for large r is implemented as

$$\frac{\partial p}{\partial r} + \frac{4}{r}p = 0 \quad \text{at } r = r_{\text{max}}. \quad (5)$$

The integral for the force can be evaluated as

$$F(t) \cong 2\pi \int_0^{r_{\text{max}}} [p(r, t) + \Pi(h(r, t))]rdr + 2\pi \int_{r_{\text{max}}}^{\infty} p(r, t)rdr, \quad (6)$$

where r_{max} has been chosen large enough to ensure that $\Pi(h(r > r_{\text{max}})) \ll 2\sigma/R$, so disjoining pressure can be ignored in the second integral and the asymptotic form of the pressure p is used to evaluate the integral directly.

A further boundary condition or constraint, the nature of which depends on the physical problem under consideration, is required to completely specify the solution. One such case is the constant force constraint that is imposed on Eq. (3) and is appropriate for interaction under gravity or buoyancy effects. This case has been considered in detail by Yiantsios and Davis.^{28,36} Another boundary condition that is commonly used in the literature is the constant velocity condition which states that at $r = r_{\text{max}}$, $\partial h / \partial t = V$, an imposed constant velocity.^{27,37} However, the modeling of measurements undertaken using the AFM and the SFA require a new boundary condition that reflects how drops interact and deform under a constant volume constraint as they are driven together or pulled apart by an externally controlled displacement as depicted in Figs. 1 and 2.

It has been shown that when a sessile drop with an equilibrium contact angle θ (see Fig. 2) and unperturbed drop height z_0 is subjected to an applied force that is localized around the apex, the perturbed drop height $z^{\text{outer}}(r)$ outside the zone in which the force acts has the following small r (on the drop scale) asymptotic form as the drop deforms under constant volume,^{11,18,38}

$$z^{\text{outer}}(r, t) \cong z_0 - \frac{r^2}{2R} + G \left[\log \left(\frac{r}{2R_d} \right) + B(\theta) \right]. \quad (7)$$

The constant $B(\theta)$ depends whether during deformation, the three phase contact line (TPL) remains *pinned* or is free to *slip* on the substrate to maintain the unperturbed contact angle θ and is given by

$$B(\theta) = \begin{cases} 1 + \frac{1}{2} \log \left(\frac{1 + \cos \theta}{1 - \cos \theta} \right), & \text{pinned TPL,} \\ 1 + \frac{1}{2} \log \left(\frac{1 + \cos \theta}{1 - \cos \theta} \right) - \frac{1}{2 + \cos \theta}, & \text{slip TPL.} \end{cases} \quad (8)$$

Equation (7) for the drop profile, which reflects the constant volume constraint on the deforming sessile drop, is an expansion correct to first order in (G/R_d) . This result together with the geometric condition (see Figs. 1 and 2),

$$X(t) = \begin{cases} h(r, t) + z(r, t), & \text{one drop (SFA),} \\ h(r, t) + z_p(r, t) + z_c(r, t), & \text{two drops (AFM),} \end{cases} \quad (9)$$

give the required boundary condition at r_{max} by a differentiation with respect to t to eliminate the constants

$$\frac{dX}{dt} = \frac{\partial h}{\partial t} + \alpha \frac{dG}{dt} \quad \text{at } r = r_{\text{max}}, \quad (10)$$

where

$$\alpha = \begin{cases} \log \left(\frac{r_{\text{max}}}{2R_d} \right) + B(\theta), & \text{one drop (SFA),} \\ 2 \log \left(\frac{r_{\text{max}}}{2\sqrt{R_c R_p}} \right) + B(\theta_c) + B(\theta_p), & \text{two drops (AFM).} \end{cases} \quad (11)$$

Equation (10) is the appropriate constant drop volume boundary condition for AFM and SFA experiments in which the variation of the displacement function $X(t)$ with time t is specified. In these experiments, the effects of driving the drops via the displacement function $X(t)$ enter as the boundary condition, Eq. (10), for the film drainage Stokes–Reynolds equation (1) and surface deformation, Eq. (2). The term adG/dt in Eq. (10) accounts for effects due to deformations of the drop outside the interaction zone under a constant volume constraint. The unperturbed contact angles θ_c and θ_p are defined in Fig. 1. For convenience of later discussions, we define

$$\Delta X(t) \equiv \begin{cases} X(t) - z_0, & \text{one drop (SFA),} \\ X(t) - z_{p0} - z_{c0}, & \text{two drops (AFM).} \end{cases} \quad (12)$$

where $\Delta X(t)=0$ corresponds to the position where mica and the mercury drop (SFA) or where the two drops (AFM) would have come into contact had the drops not deformed.

In the SFA experiment when the mica plate is pushed towards the mercury drop for a time interval and then stops (see Fig. 2), whereupon $dX/dt=0$ thereafter, we expect $\partial h/\partial t$ will also vanish at r_{\max} so we will have $dG/dt=0$ as well from Eq. (10). So from Eq. (3) we can see that after the mica stops, the system will evolve as a constant force system as it approaches equilibrium.

The governing equations (1)–(6) and Eqs. (8)–(11) can be solved by the method of lines through central difference discretization in r . Since the force, Eq. (3), enters in the new boundary condition, Eq. (10), we have a system of differential-algebraic equations. With the scaling (based on the capillary number $Ca = \mu V/\sigma$), $h_c = R_0 Ca^{1/2}$, $r_c = R_0 Ca^{1/4}$, $p_c = \sigma/R_0$ and $t_c = \mu Ca^{-1/2}/p_c$ we can achieve more than seven digit precision with a scaled grid size in $r=0.02$ and a scaled $r_{\max}=10-15$. The system of typically around 500 equations can be solved by using the MATLAB routine `ode15s`.¹⁸ The domain size of our numerical scheme satisfies $r_{\max}/R_0 < 0.3$ and the value of r_{\max} is checked to ensure that deformations and forces are independent of its precise value. Thus we can see from Eq. (10) that if $dX/dt = -V$ (a constant), then the constant velocity boundary condition $\partial h/\partial t = -V$ is only valid if $r_{\max} = r_1$, the radius of the capillary tube in the SFA experiment.

Before we obtain numerical solutions of the governing equations of the model and compare with experimental results we can obtain two limiting solutions that are valid for small and large forces at low velocities.

B. Approximate analytical results

While the numerical solution of the governing equations (1)–(11) can be readily obtained, a certain amount of familiarity with numerical analysis and software tools is required. This section presents relatively simple and accurate approximate analytical results for the physically interesting and important force-displacement relationships for both small and large forces. These formulas are validated by comparison with full numerical solutions in the next section.

We first provide a result applicable for small forces when deformations of the interfaces are small. In the AFM and

SFA experiments the capillary number $Ca < 10^{-5}$. We scale all physical variables using³⁷ $\{G, \Delta X, h\} \sim (Ca^{1/2} R)$, $r \sim (Ca^{1/4} R)$, $\{p, \Pi\} \sim (\sigma/R)$, $t \sim (Ca^{-1/2} R\mu/\sigma)$ and seek a solution for the nondimensional film thickness of the form

$$h(r, t) = a(t) + \beta r^2 \quad (13)$$

to obtain an expression for the dynamic force, $F(t)$ defined by Eq. (3), in physical units,

$$F(t) = -6\pi R\sigma Ca^{1/2} df/dt, \quad (14)$$

where $f(t) = \log(a(t))$ and the function $a(t)$ obeys the following differential equation:

$$\frac{3}{a(t)} \frac{da(t)}{dt} \left[B(\theta) + \log(Ca^{1/4}/2) + \frac{1}{2} \log(2a(t)) \right] - a(t) = -\Delta X(t) \quad (\text{SFA}), \quad (15a)$$

$$\frac{3}{4a(t)} \frac{da(t)}{dt} \left[B(\theta_c) + B(\theta_p) + 2 \log(Ca^{1/4}/2) + \frac{1}{2} \log(a(t)) \right] - a(t) = -\Delta X(t) \quad (\text{AFM}). \quad (15b)$$

The derivation of this result is given in Appendices A and B. The range of applicability of this result can be seen by comparing against the full numerical solution in Fig. 6 below.

When the dynamic deformation of the interacting surfaces is large, we can identify a film radius, r_f which characterizes the extent of flattening of the surface due to interactions. This radius is given by (see Appendix C)

$$r_f \approx \left[\frac{R_f}{\sigma} \int_0^\infty (p + \Pi) r dr \right]^{1/2} = \sqrt{GR_f} \quad (16)$$

so that the dynamic pressure profile can be approximated by

$$(p + \Pi) \approx \begin{cases} (2\sigma/R_f), & 0 < r < r_f, \\ 0, & r > r_f. \end{cases} \quad (17)$$

With this simplified picture of the surface deformation and pressure profile, we obtain the desired result that links two experimental quantities: the displacement $\Delta X(t)$ and the force $F(t)$ (see Appendix C),

$$\Delta X \equiv h_f + \frac{F}{4\pi\sigma} \left[\log\left(\frac{FR_0}{8\pi\sigma R_d^2}\right) + 2B(\theta) - 1 \right] \quad \text{one drop (SFA),} \quad (18a)$$

$$\Delta X \equiv h_f + \frac{F}{2\pi\sigma} \left[\log\left(\frac{F}{8\pi\sigma\sqrt{R_c R_p}}\right) + B(\theta_c) + B(\theta_p) - 1 - \frac{2\pi\sigma}{K} \right] \quad \text{two drops (AFM).} \quad (18b)$$

The constant thickness h_f is an approximate attempt to account for the fact that the force will start to be significant

when the surfaces are at h_f apart (where $\Delta X = h_f$) rather than at $\Delta X = 0$, when the surfaces would have come into contact without deformation.

An important observation about Eq. (18) is the nonlinear nature of the force-displacement relationship over the typical range force magnitudes. Also this force-displacement relationship depends on properties of the drop such as the undeformed drop radius, interfacial tension, contact angle, the particle radius, as well as whether the three phase contact line is pinned or is free to slip via the function, $B(\theta)$. This has implications in any attempt to locate the constant compliance region of AFM results. Earlier work on the interpretation of direct force measurements involving drops and bubbles assumed that they deform as Hookean springs.^{1,39}

III. RESULTS

A. Approximate formulas: SFA geometry

We compare the extent to which the approximate results for small forces equation (14) and large forces equation (18) are able to model the force-displacement curves due to hydrodynamic interactions for the case of a single drop against a moving flat plate in the SFA configuration as given by the model described by Eqs. (1)–(12). Disjoining pressure effects have not been included in this comparison.

In Fig. 3(a), we compare the large force analytic formula given by Eq. (18a) with the numerical solution of Eqs. (1)–(12) for the approach of a mica plate at constant velocity ($V = 24 \mu\text{m/s}$) towards a mercury drop. The mica plate is driven to $17.5 \mu\text{m}$ beyond the point at which the mica would have made contact with the mercury drop if the drop did not deform ($\Delta X = -17.5 \mu\text{m}$). We see that the analytic formula tracks the full numerical results closely for $\Delta X \leq -5 \mu\text{m}$.

To assess the accuracy of the small force result given by Eqs. (14) and (15a), the mica plate is driven towards the mercury drop at $24 \mu\text{m/s}$ until $\Delta X = 0$ (where the surfaces would have touched if the mercury did not deform), and is then retracted at the same speed. In Fig. 3(b) we can see that all the key features of the force-displacement curve, including the force maximum at $\Delta X = 0$ and the depth and position of the attractive minimum in the retraction branch are reproduced quantitatively by the approximate formula. For comparison, the constant velocity Reynolds formula applicable to rigid spheres, $F = 6\pi\mu R^2 V / \Delta X = 6\pi\mu R^2 V / [X(0) - Vt]$, which diverges at $\Delta X = 0$ is also given. This comparison validates the utility of the simple approximate small force result in replicating quantitative and qualitative features of the force versus displacement result without the need to obtain a more complicated full numerical solution.

B. Comparison with SFA experiments

An assessment of the model given in Eqs. (1)–(12) in predicting measured time evolution of the deformations of a mercury/electrolyte interface due to an approaching mica plate at constant velocity is given in Fig. 4. We see that for the system with disjoining pressures detailed in Fig. 1 the model performs equally well in the presence of a strongly repulsive (SR) disjoining pressure between the mica and the

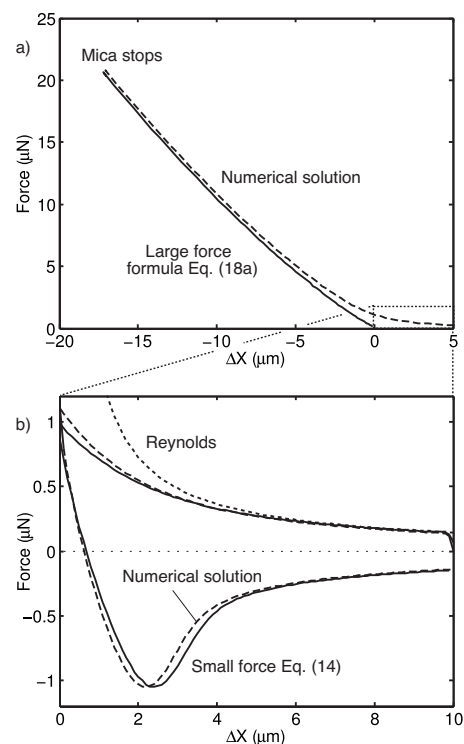


FIG. 3. Comparison of approximate results (solid lines) for large [Eq. (18a)] and small forces [Eqs. (14) and (15a)] with full numerical solution (broken lines) for the force against mica displacement between a single mercury drop (surface tension 420 mN/m , undeformed radius of curvature 1.9 mm) interacting with a flat mica plate in the SFA geometry across water driven at a constant velocity of $24 \mu\text{m/s}$. (a) The mica plate is driven to a position $17.5 \mu\text{m}$ beyond the position where the mica and the mercury would have made contact if the mercury did not deform (i.e., $\Delta X = -17.5 \mu\text{m}$) and $h_f = 0$. (b) The mica plate is driven to $\Delta X = 0$ and is then retracted at the same speed. There is no disjoining pressure term between the mica and the mercury interface. The constant velocity Reynolds result (dotted line) is also included for comparison.

mercury that leads to an equilibrium flat film when the mica stops, or in the presence of a strongly attractive (SA) disjoining pressure that lead to an unstable film that ultimately collapses as the mercury jumps into contact with the mica plate. Similar results have been presented previously.²⁴

From the film profiles, the total force between the mica and the deformable mercury drop can be calculated and separated into contributions from hydrodynamic and disjoining pressure contributions.²² In Figs. 5(a) and 5(b) we can see excellent agreement between the force components predicted from theory and deduced experimentally. This is not surprising since the profiles as seen in Fig. 4 are in excellent agreement. It is interesting to note that until the mica stops, after which the mercury interface of the strongly attractive case collapses onto the mica, the force as a function of time is nearly identical between the strongly repulsive and the strongly attractive cases [Fig. 5(c)]. Indeed this portion of the force curve is also well described by the large force formula, Eq. (18a).

The results in Fig. 5(c) also demonstrate that after the mica stops, the interface in the strongly repulsive case evolves towards the equilibrium film under constant force as pointed out in Sec. II A. To leading order, the value of the

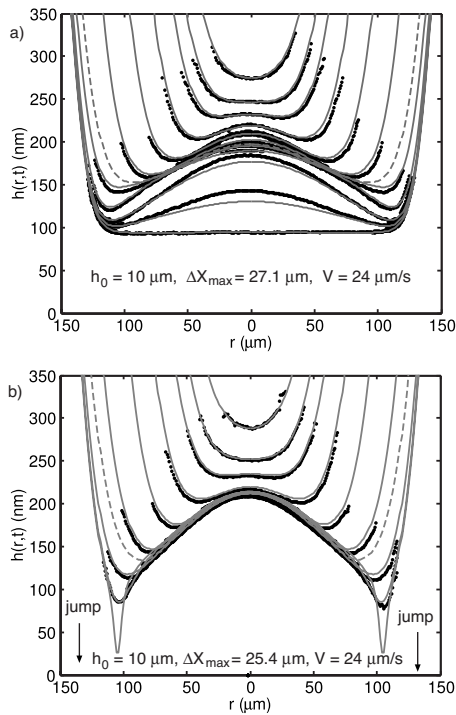


FIG. 4. Comparisons between numerical solutions of Eqs. (1)–(12) (lines) and SFA experiments (symbols) of the profile of an aqueous film between a deformable mercury drop and an approaching mica plate at constant velocity V for (a) strongly repulsive (SR) disjoining pressures at $t = -0.02, 0.02, 0.06, 0.14, 0.26, 0.42, 0.555$ (dashed curve, without data points—mica stops), $0.62, 0.82, 1.62, 3.62,$ and 13.62 s. (b) Strongly attractive (SA) disjoining pressures at $t = -0.02, 0.02, 0.06, 0.14, 0.26, 0.42, 0.5$ (dashed curve, without data points—mica stops), $0.58,$ and 0.64 s. The point $t=0$ is defined to be the time at which the curvature of the profile at $r=0$ changes sign, h_0 is the initial distance of closest approach between the mica and the mercury and ΔX_{\max} is the maximum displacement of the mica plate. See Fig. 1 for details of system parameters (Refs. 21 and 24).

constant force is approximately equal to the Laplace pressure of the drop multiplied by the film radius which is approximately constant [curves (d)–(g) in the inset of Fig. 5(c)] after the mica stops. As the deformation of the drop remains small compared to the drop dimension, the Laplace pressure remains essentially constant.

C. Comparison with AFM experiments

We now compare predictions of the force calculated from Eqs. (1)–(12) as well as from the approximate formula for small forces [Eqs. (14) and (15b)] and large forces [Eq. (18b)] with an example of the dynamic force between two oil drops with adsorbed sodium dodecyl sulfate (SDS) as measured on the AFM at a relatively low drive velocity of $2 \mu\text{m/s}$.¹⁹ Other relevant system and input parameters are $R_c = 41 \mu\text{m}$, $R_p = 90 \mu\text{m}$, $\theta_c = 100^\circ$, $\theta_p = 50^\circ$, $h_f = 26 \text{ nm}$, $h_{\text{start}} = 1.81 \mu\text{m}$, $\Delta X_{\max} = 2 \mu\text{m}$, $\sigma = 10 \text{ mN/m}$, surface potential $\Psi_0 = -100 \text{ mV}$, Debye length $\kappa^{-1} = 3.3 \text{ nm}$, and $\text{Ca} = 1.8 \times 10^{-7}$.

From Fig. 6 we see that for $\Delta X \geq 0$, the small force approximation given by Eqs. (14) and (15b) is very close to the full numerical solution and to the experimental data. For $F \geq 1 \text{ nN}$, the large force analytic result, Eq. (18b), becomes applicable. The full numerical solution of the governing

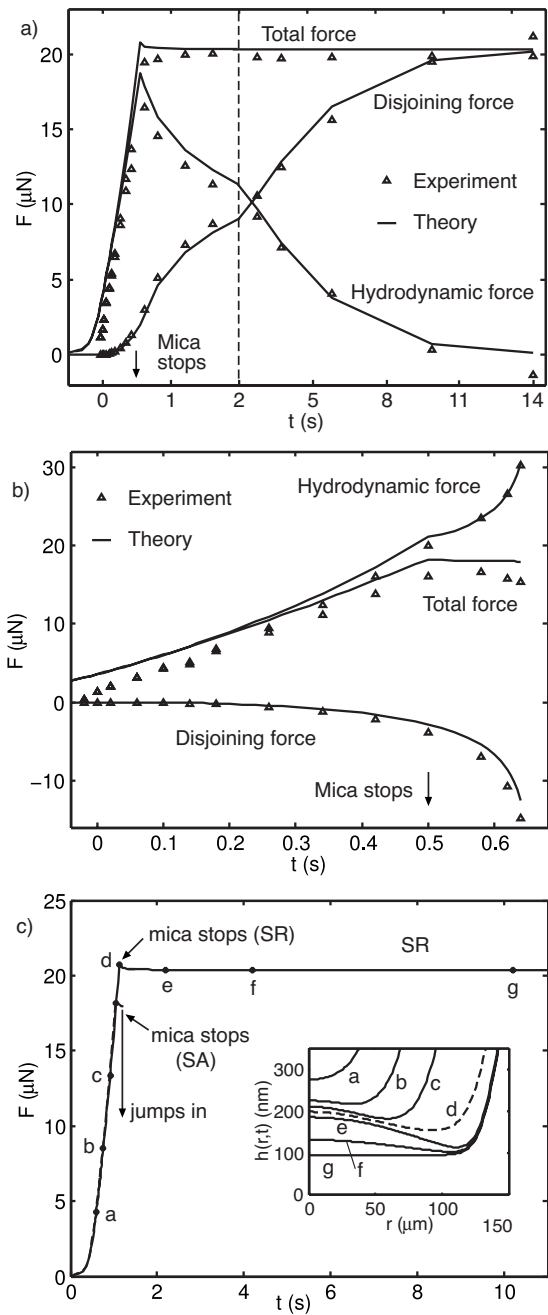


FIG. 5. Comparisons between numerical solutions of Eqs. (1)–(12) (lines) and SFA experimental (symbols) determinations of components of the total force as a function of time for (a) the strongly repulsive (SR) disjoining pressure (note the change in scale on the time axis at $t=2$ s). (b) Strongly attractive (SA) disjoining pressures. The time at which the mica stops is indicated by the vertical arrow. (c) An illustration that the force between the SR and SA cases are nearly identical until the mica stops when the SA system jumps into contact while the SR case continues to evolve to the equilibrium film under a constant force condition—from point (d) when the mica stops to point (g).

equation is in excellent agreement with experimental results at all displacements. As the drive velocity increases, the full numerical solution becomes necessary in bridging the transition region between the low force limit and the moderate deformation regime. One should also bear in mind that the governing equations given by Eqs. (1)–(12) have been obtained under a small strain assumption, as defined by

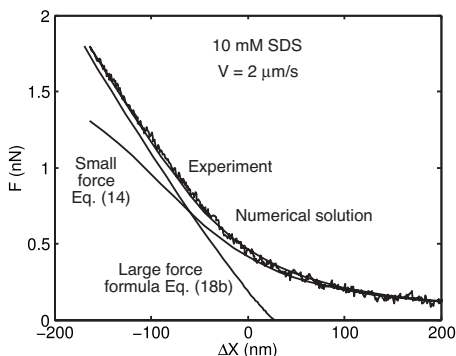


FIG. 6. Comparisons between the numerical solution of Eqs. (1)–(12) which lies on top of experimental forces measured on the AFM between two decane drops on approach, the large force formula given by Eq. (18b) and the small forces result given by Eqs. (14) and (15b). The drive velocity is $2 \mu\text{m/s}$. The disjoining pressure due to electrical double layer interactions between the drops is repulsive (Ref. 19).

$(F/2\pi\sigma R) \ll 1$ (see also Sec. IV). Fortunately current AFM and SFA measurements fall within this regime.

IV. DISCUSSION

The AFM and SFA experiments probe the behavior involving deforming interfaces on very different scales. For example the characteristic drop sizes are of order micrometer in the AFM and millimeter in the SFA experiments. The forces involved also differ by three orders of magnitude: nN for the AFM and μN for the SFA. Also the interfacial tensions: oil/water and mercury/water, differ by two orders of magnitude. However, the two types of experiments are similar when viewed on an appropriate scale.

In both cases, the deformation of the interface on the macroscopic scale is characterized by ΔX and there is a characteristic length associated with the interaction force, F and the interfacial tension σ , $G = F/2\pi\sigma$. Dimensional analysis expects a functional relationship between the dimensionless ratio (G/R) and the strain $(\Delta X/R)$ that can also depend on the contact angle θ . In Fig. 7, it is evident where the AFM and SFA experimental systems reside in this scaled domain.

The effects of varying the drive velocity, V in AFM force measurement and the associated variations with the capillary number ($\text{Ca} = \mu V/\sigma$) are demonstrated in Fig. 8. We observe

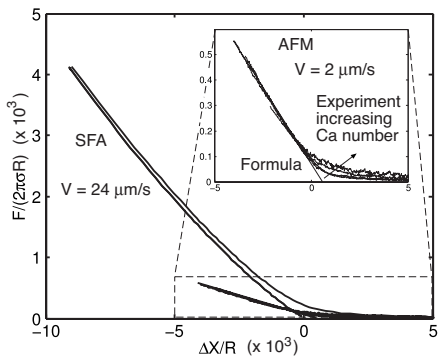


FIG. 7. Comparisons between AFM and SFA forces on the same scale. The inset provides details due to variations in the capillary number, Ca .

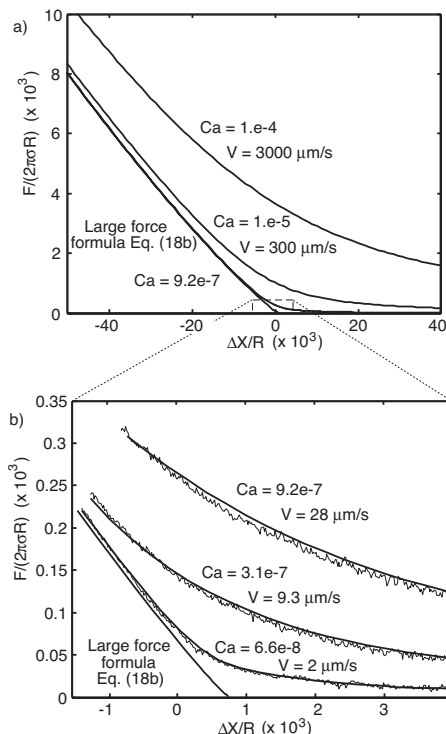


FIG. 8. AFM results plotted on the dimensionless force-strain scale. (a) For such experiments, unrealistically large drive velocities still correspond to small capillary numbers, Ca . (b) Comparison with AFM experimental results at 1 mM SDS. The large force result [Eq. (18b)] is applicable to low velocities or $\text{Ca} \lesssim 10^{-7}$. The full numerical solution is required to describe results at higher capillary numbers.

that the large force formula [Eq. (18b)] is applicable for $\Delta X/R \leq 0$ at low velocities $\leq 2 \mu\text{m/s}$ or $\text{Ca} \lesssim 10^{-7}$, while the full numerical solution of Eqs. (1)–(12) is required to describe results at higher capillary numbers.

Finally we demonstrate the effects of contact angle in SFA (one drop) and AFM configurations (two drops, assuming identical contact angles) on the dependence of the force on the displacement in Fig. 9 in the limit of zero capillary number. With increasing contact angle, the drop(s) become more compliant which results in a lower scaled force for the same value of the scaled strain or deformation ($\Delta X/R$).

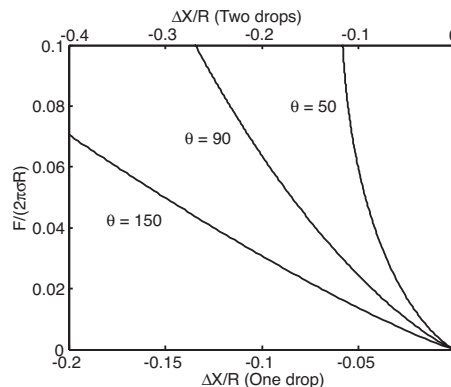


FIG. 9. Variations of the scaled force with scaled deformation for the AFM (two drops, identical contact angles) and SFA (one drop) configurations at zero capillary number.

In this study we have demonstrated the utility of a model based on the Stokes–Reynolds theory of thin film drainage and the Young–Laplace equation of drop deformation that can provide accurate descriptions of force measurement and deformation studies based on the AFM and the SFA. A key element of the model is that the constant volume constraint of interacting drops gives rise to a new boundary condition for the set of partial differential equations. Two simple analytic limits of this model have been derived. One is applicable at large separations and small forces for which contributions of the disjoining pressure can be neglected and the other is applicable at large force but at low capillary numbers or drive velocities where a stable dynamic film forms between the interacting interfaces. While the model is essentially a small strain model, it has been demonstrated that it covers the practical range of direct force measurement based on this family of apparatus. Fortunately, this regime also covers the domain of interactions of interest in typical droplet and emulsion interactions. The model also assumes that the deformable interface can be modeled by a constant interfacial tension. This can be justified as follows. In the AFM force measurements between decane drops stabilized by the charged surfactant sodium dodecyl sulfate, the surfactant concentration is high, near the critical micelle concentration. As such the oil/water interface is fully populated by surfactants which then renders the interface to be “immobile” in the traditional hydrodynamic sense. Also in the low capillary number regime of these experiments, tangential stress due to hydrodynamic flow are four orders of magnitude smaller than the surface pressure of surfactant at such concentrations. For the mercury/electrolyte interface, the interfacial tension is over 40 times higher than the decane/water system. We also find that the measured time dependence of the surface deformation can only be accounted for by a no-slip boundary condition. This observation is consistent with studies of the electrokinetic properties of mercury drops where an apparent no-slip condition can be shown to be the result of the (highly) charged nature of the mercury/electrolyte interface.^{30–32}

The present detailed modeling effort of deformations and hydrodynamic drainage on the nanoscale can be extended to applications where the hydrodynamic conditions are more vigorous, as for example, in mineral flotation applications, where there may be large scale deviations of the drop geometry from sphericity. A possible approach may be along the lines of a recent study⁴⁰ but with a more detailed matching of the outer boundary condition of the thin film domain to large deformations of a moving drop or bubble, as we have done

here by matching with a physical constraint of constant volume.

ACKNOWLEDGMENTS

This work has been supported in part by the Australian Research Council (ARC) through the Particulate Fluids Processing Center and the Ian Wark Research Institute, both of which are ARC Special Research Centers. R.M. is supported by a University of Melbourne International Research Scholarship. D.Y.C.C. is also supported by a Visiting Professorship at the National University of Singapore.

APPENDIX A: FORMAL RESULTS

We first derive some formal results from the governing equations relevant to both the SFA (one drop) and the AFM (two drops) configuration. Equation (1) can be integrated formally to give

$$p(r,t) = -12\mu \int_r^\infty \frac{ds}{sh^3(s,t)} \int_0^s x \frac{\partial h(x,t)}{\partial t} dx \quad (\text{A1})$$

and Eqs. (2a) (in the flat plate limit, $R_s \rightarrow \infty$) and (2b) can also be integrated to give the inner solution

$$\beta h^{\text{inner}}(r,t) = \beta h(0,t) + \frac{r^2}{2R} + \frac{1}{\sigma} \int_0^r s \log(s/r) [p + \Pi] ds, \quad (\text{A2})$$

where the constant $\beta=1$ for the one drop against a flat plate geometry [SFA equation (2a)] and $\beta=1/2$ for the two drop geometry [AFM equation (2b)]. Now $p(r,t)$ can be eliminated from Eqs. (A1) and (A2) to give the formal but exact result

$$\begin{aligned} \beta h^{\text{inner}}(r,t) = & \beta h(0,t) + \frac{r^2}{2R} + \frac{1}{\sigma} \int_0^r s \log(s/r) \Pi ds \\ & - \frac{6\mu}{\sigma} \int_0^r \frac{s \log(s/r) ds}{h^3(s,t)} \int_0^s x \frac{\partial h(x,t)}{\partial t} dx \\ & + \frac{3\mu}{\sigma} \int_0^r \frac{s ds}{h^3(s,t)} \int_0^s x \frac{\partial h(x,t)}{\partial t} dx \\ & + \frac{3\mu}{\sigma} r^2 \int_0^r \frac{ds}{sh^3(s,t)} \int_0^s x \frac{\partial h(x,t)}{\partial t} dx. \end{aligned} \quad (\text{A3})$$

When r is large compared to the radial extent of the film, this inner solution matches the outer solution that follows from Eqs. (7), (9), and (12),

$$h^{\text{outer}}(r,t) = \begin{cases} \Delta X(t) + \frac{r^2}{2R} - G \left[\log\left(\frac{r}{2R_d}\right) + B(\theta) \right] & \text{one drop (SFA),} \\ \Delta X(t) + \frac{r^2}{R} - G \left[2 \log\left(\frac{r}{2\sqrt{R_c R_p}}\right) + B(\theta_c) + B(\theta_p) \right] & \text{two drops (AFM),} \end{cases} \quad (\text{A4})$$

and we can identify the coefficient of $\log(r)$ as

$$G(t) = -\frac{6\mu}{\sigma} \int_0^\infty \frac{s ds}{h^3(s,t)} \int_0^s r \frac{\partial h(r,t)}{\partial t} dr + \frac{1}{\sigma} \int_0^\infty r \Pi dr, \quad (\text{A5})$$

which from Eq. (A1), is equivalent to the definition of the force given in Eq. (3).

APPENDIX B: SMALL FORCE LIMIT

We can develop a solution valid for weak interactions that include hydrodynamic interactions and surface deformations but omitting effects due to disjoining pressure. The result is expected to be accurate for $\Delta X > 0$ before surface forces become important. We first scale variables using the capillary number $\text{Ca} = (\mu V / \sigma)$,³⁷ $\{G, \Delta X, h\} \sim (\text{Ca}^{1/2} R)$, $r \sim (\text{Ca}^{1/4} R)$, $\{p, \Pi\} \sim (\sigma/R)$, $t \sim (\text{Ca}^{-1/2} R \mu / \sigma)$ and use a trial solution of the (nondimensional) form

$$h(r,t) = a(t) + \beta r^2 \quad (\text{B1})$$

on the right-hand side of Eq. (A3) to construct the inner solution. While the trial solution assumes that the film profile has a parabolic shape, the inner solution given by Eq. (A3) will contain the requisite logarithmic term to match with the outer solution, Eq. (A4). To determine the unknown function $a(t)$ we substitute Eq. (B1) into the right-hand side of Eq. (A3), take the $r \rightarrow \infty$ limiting form to match the result to the outer solution Eq. (A4). This matching gives a first order differential equation for $a(t)$,

$$\frac{3}{a(t)} \frac{da(t)}{dt} \left[B(\theta) + \log(\text{Ca}^{1/4}/2) + \frac{1}{2} \log(2a(t)) \right] - a(t) = -\Delta X(t) \quad (\text{SFA}), \quad (\text{B2a})$$

$$\frac{3}{4a(t)} \frac{da(t)}{dt} \left[B(\theta_c) + B(\theta_p) + 2 \log(\text{Ca}^{1/4}/2) + \frac{1}{2} \log(a(t)) \right] - a(t) = -\Delta X(t) \quad (\text{AFM}). \quad (\text{B2b})$$

By setting $f(t) = \log(a(t))$ the numerical solution of Eq. (B2) is straightforward to determine and the force, Eq. (6), can be expressed in terms of this dimensionless function $f(t)$, which is a function of the dimensionless time according to the scaling

$$F = -6\pi R \sigma \text{Ca}^{1/2} \frac{df}{dt}. \quad (\text{B3})$$

The range of applicability of this approximation is demonstrated in Sec. III.

APPENDIX C: LARGE FORCE LIMIT

We can derive a simple analytic expression for the force-displacement relationship valid for large forces (in the context of surface force measurements) when the dynamic interaction is repulsive between a solid particle and a drop. For a sessile drop subjected to an applied pressure distribution (p

+ Π) localized axisymmetrically about the apex as depicted in Fig. 2, the drop height $z(r,t)$ obeys the modified Young–Laplace equation

$$\frac{\sigma}{r} \frac{\partial}{\partial r} \left\{ \frac{r(\partial z / \partial r)}{[1 + (\partial z / \partial r)^2]^{1/2}} \right\} = (p + \Pi) - \frac{2\sigma}{R}. \quad (\text{C1})$$

On a radial scale that is small compared to the drop radius, the denominator may be replaced by unity and the resulting equation can be integrated to obtain the large r (on the scale of the radial extent of the film) limiting form of this inner solution

$$z^{\text{inner}}(r,t) \cong z(0,t) - \frac{r^2}{2R} - H + G \log(r), \quad (\text{C2})$$

where $z(0,t)$ is the perturbed drop height at $r=0$,

$$H(t) = \frac{1}{\sigma} \int_0^\infty [p(r,t) + \Pi(r,t)] r \log(r) dr \quad (\text{C3})$$

and G is given by Eq. (3). The requirement for the small r limit of the outer solution, Eq. (7), to match with the large r limit of the inner solution, Eq. (C2), gives an expression for the deformation of the drop apex

$$z_0 - z(0,t) = -H - G \left[\log\left(\frac{1}{2R_d}\right) + B(\theta) \right]. \quad (\text{C4})$$

We can integrate the equation for the film thickness, h given by Eq. (2a) to give ($R_f^{-1} \equiv R^{-1} + R_s^{-1}$),

$$r \frac{\partial h}{\partial r} = \frac{r^2}{R_f} - \frac{1}{\sigma} \int_0^r (p + \Pi) r' dr'. \quad (\text{C5})$$

When ($p + \Pi$) is repulsive, a dynamic film of constant thickness h_f forms between the drop and the solid particle. The value of h_f can be estimated by setting the right-hand side of Eq. (2) to 0. The drop is flattened against the solid particle, $\partial h / \partial r \sim 0$ on the scale of the drop radius and we can define the film radius, r_f to be the value of r at which $\partial h / \partial r$ starts to increase on the scale of the drop radius. From the right-hand side of Eq. (C5) we can identify an approximate value of the film radius, r_f by the radial position when the slope of the film profile begins to increase rapidly on the scale of the drop

$$r_f \approx \left[\frac{R_f}{\sigma} \int_0^\infty (p + \Pi) r dr \right]^{1/2} = \sqrt{GR_f} \quad (\text{C6})$$

so the dynamic pressure distribution within this film can be approximated by

$$(p + \Pi) \approx \begin{cases} (2\sigma/R_f), & 0 < r < r_f, \\ 0, & r > r_f. \end{cases} \quad (\text{C7})$$

Using this approximation in Eq. (C4) gives an approximate expression for the drop deformation in terms of the force, F ,

$$z_0 - z(0,t) \cong -\frac{F}{4\pi\sigma} \left[\log\left(\frac{FR_0}{8\pi\sigma R_d^2}\right) + 2B(\theta) - 1 \right], \quad (\text{C8})$$

where to leading order in (G/R_d) we have made the approximation $R_f^{-1} \equiv R^{-1} + R_s^{-1} \approx R_d^{-1} + R_s^{-1} \equiv R_0^{-1}$.

From the definition of the displacement function $\Delta X(t)$ in Eq. (12) we now have the desired results between the two measurable experimental quantities: the displacement, $\Delta X(t)$ and the force, F ,

$$\Delta X \cong h_f + \frac{F}{4\pi\sigma} \left[\log\left(\frac{FR_0}{8\pi\sigma R_d^2}\right) + 2B(\theta) - 1 \right] \quad \text{one drop (SFA)}. \quad (\text{C9a})$$

The constant dynamic film thickness h_f has been added to the right-hand side as an approximate attempt to account for the fact that the force will start to be significant when the surfaces are at h_f apart, where $\Delta X = h_f$, rather than at $\Delta X = 0$, when the surfaces would have come into contact without deformation.

The one drop SFA result corresponds to the limit of the particle radius, $R_s \rightarrow \infty$, or $R_0 \rightarrow R_d$, the undeformed radius of the drop. With the appropriate expression for $B(\theta)$ from Eq. (8), the result in Eq. (C9a) is valid for both the pinned or free to slip three phase contact line condition and for acute or obtuse contact angles, θ .

A similar derivation gives the corresponding result for the force-displacement relation for two drops in the AFM for which we have to account for the deflection of the cantilever with spring constant K (see Fig. 1),

$$\Delta X \cong h_f + \frac{F}{2\pi\sigma} \left[\log\left(\frac{F}{8\pi\sigma\sqrt{R_c R_p}}\right) + B(\theta_c) + B(\theta_p) - 1 - \frac{2\pi\sigma}{K} \right] \quad \text{two drops (AFM)}. \quad (\text{C9b})$$

In practice the deflection of the cantilever is often taken into account before the data are analyzed for force-displacement effects.

¹W. A. Ducker, Z. Xu, and J. N. Israelachvili, "Measurements of hydrophobic and DLVO forces in bubble-surface interactions in aqueous solutions," *Langmuir* **10**, 3279 (1994).
²H.-J. Butt, "A technique for measuring the force between a colloidal particle in water and a bubble," *J. Colloid Interface Sci.* **166**, 109 (1994).
³M. L. Fielden, R. Hayes, and J. Ralston, "Surface and capillary forces affecting air bubble particle interactions in aqueous electrolyte," *Langmuir* **12**, 3721 (1996).
⁴M. Preuss and H.-J. Butt, "Direct measurement of particle-bubble interactions in aqueous electrolyte: dependence on surfactant," *Langmuir* **14**, 3164 (1998).
⁵S. Basu and M. M. Sharma, "Measurement of critical disjoining pressure for dewetting of solid surfaces," *J. Colloid Interface Sci.* **181**, 443 (1996).
⁶P. Mulvaney, J. M. Perera, S. Biggs, F. Grieser, and G. W. Stevens, "The direct measurement of the forces of interaction between a colloid particle and an oil droplet," *J. Colloid Interface Sci.* **183**, 614 (1996).
⁷B. A. Snyder, D. E. Aston, and J. C. Berg, "Particle-drop interaction examined with an atomic force microscope," *Langmuir* **13**, 590 (1997).
⁸P. G. Hartley, F. Grieser, P. Mulvaney, and G. W. Stevens, "Surface forces and deformation at the oil-water interface probed using AFM force measurement," *Langmuir* **15**, 7282 (1999).
⁹D. E. Aston and J. C. Berg, "Quantitative analysis of fluid interface-atomic force microscopy," *J. Colloid Interface Sci.* **235**, 162 (2001).
¹⁰D. Bhatt, J. Newman, and C. J. Radke, "Equilibrium force isotherms of a deformable bubble/drop interacting with a solid particle across a thin liquid film," *Langmuir* **17**, 116 (2001).
¹¹D. Y. C. Chan, R. R. Dagastine, and L. R. White, "Force between a rigid probe particle and a liquid interface I. The repulsive case," *J. Colloid Interface Sci.* **236**, 141 (2001).

¹²S. A. Nespolo, D. Y. C. Chan, F. Grieser, P. G. Hartley, and G. W. Stevens, "Forces between a rigid probe particle and a liquid interface: comparison between experiment and theory," *Langmuir* **19**, 2124 (2003).
¹³R. R. Dagastine, D. C. Prieve, and L. R. White, "Forces between a rigid probe particle and a liquid interface III. Extraction of the planar half-space interaction energy (ED)," *J. Colloid Interface Sci.* **269**, 84 (2004).
¹⁴G. Gillies and C. A. Prestidge, "Interaction forces, deformation and nano-rheology of emulsion droplets as determined by colloid probe AFM," *Adv. Colloid Interface Sci.* **108**, 197 (2004).
¹⁵D. E. Aston and J. C. Berg, "Thin-film hydrodynamics in fluid interface-atomic force microscopy," *Ind. Eng. Chem. Res.* **41**, 389 (2002).
¹⁶R. R. Dagastine, G. W. Stevens, D. Y. C. Chan, and F. Greiser, "Forces between two oil drops in aqueous solution measured by AFM," *J. Colloid Interface Sci.* **273**, 339 (2004).
¹⁷R. R. Dagastine, T. T. Chau, D. Y. C. Chan, G. W. Stevens, and F. Greiser, "Interaction forces between oil-water particle interfaces—non-DLVO forces," *Faraday Discuss.* **129**, 111 (2005).
¹⁸S. L. Carnie, D. Y. C. Chan, C. Lewis, R. Manica, and R. R. Dagastine, "Measurement of dynamical forces between deformable drops using the atomic force microscope. I. Theory," *Langmuir* **21**, 2912 (2005).
¹⁹R. R. Dagastine, R. Manica, S. L. Carnie, D. Y. C. Chan, G. W. Stevens, and F. Grieser, "Dynamic forces between two deformable oil droplets in water," *Science* **313**, 210 (2006).
²⁰J. N. Connor and R. G. Horn, "Measurement of aqueous film thickness between charged mercury and mica surfaces: A direct experimental probe of the Poisson-Boltzmann distribution," *Langmuir* **17**, 7194 (2001).
²¹J. N. Connor and R. G. Horn, "The influence of surface forces on thin film drainage between a fluid drop and a flat solid," *Faraday Discuss.* **123**, 193 (2003).
²²R. G. Horn, M. Asadullah, and J. N. Connor, "Thin film drainage: hydrodynamic and disjoining pressures determined from experimental measurements of the shape of a fluid drop approaching a solid wall," *Langmuir* **22**, 2610 (2006).
²³S. L. Carnie, D. Y. C. Chan, and R. Manica, "Modelling drop-drop interactions in an atomic force microscope," *ANZIAM J.* **46**, C805 (2005).
²⁴R. Manica, J. N. Connor, S. L. Carnie, R. G. Horn, and D. Y. C. Chan, "Dynamics of interactions involving deformable drops: Hydrodynamic dimpling under attractive and repulsive electrical double layer interactions," *Langmuir* **23**, 626 (2007).
²⁵R. Manica, J. N. Connor, L. Y. Clasohm, S. L. Carnie, R. G. Horn, and D. Y. C. Chan, "Transient responses of a wetting film to mechanical and electrical perturbations," *Langmuir* **24**, 1381 (2008).
²⁶D. McCormack, S. L. Carnie, and D. Y. C. Chan, "Calculations of electric double-layer force and interaction free energy between dissimilar surfaces," *J. Colloid Interface Sci.* **169**, 177 (1995).
²⁷S. Abid and A. K. Chesters, "The drainage and rupture of partially-mobile film between colliding drops at constant approach velocity," *Int. J. Multiphase Flow* **20**, 613 (1994).
²⁸S. G. Yiantsios and R. H. Davis, "On the buoyancy-driven motion of a drop towards a rigid surface or a deformable interface," *J. Fluid Mech.* **217**, 547 (1990).
²⁹S. A. Nespolo, M. A. Bevan, D. Y. C. Chan, F. Grieser, and G. W. Stevens, "Hydrodynamic and electrokinetic properties of decane droplets in aqueous sodium dodecyl sulfate solutions," *Langmuir* **17**, 7210 (2001).
³⁰V. G. Levich, *Physicochemical Hydrodynamics* (Prentice-Hall, Englewood Cliffs, NJ, 1962).
³¹H. Ohshima, T. W. Healy, and L. R. White, "Electrokinetic phenomena in a dilute suspension of charged mercury drops," *J. Chem. Soc., Faraday Trans. 2* **80**, 1643 (1984).
³²H. Ohshima, "Primary electroviscous effect in a dilute suspension of charged mercury drops," *Langmuir* **22**, 2863 (2006).
³³C.-Y. Lin and J. C. Slattery, "Thinning of a liquid film as a small drop or bubble approaches a fluid-fluid interface," *AIChE J.* **28**, 786 (1982).
³⁴J.-D. Chen, "Effect of London-van der Waals and electric double layer forces on the thinning of a dimpled film between a small drop or bubble and a horizontal solid plane," *J. Colloid Interface Sci.* **98**, 329 (1984).
³⁵A. Saboni, C. Gourdon, and A. K. Chesters, "Drainage and rupture of partially mobile films during coalescence in liquid-liquid systems under a constant interaction force," *J. Colloid Interface Sci.* **175**, 27 (1995).
³⁶S. G. Yiantsios and R. H. Davis, "Close approach and deformation of two viscous drops due to gravity and van der Waals forces," *J. Colloid Interface Sci.* **144**, 412 (1991).

- ³⁷E. Klaseboer, J. P. Chevaillier, C. Gourdon, and O. Masbernat, "Film drainage between colliding drops at constant approach velocity: experiments and modeling," *J. Colloid Interface Sci.* **229**, 274 (2000).
- ³⁸D. C. Bardos, "Contact angle dependence of solid probe-liquid drop forces in AFM measurements," *Surf. Sci.* **515**, 157 (2002).
- ³⁹P. Attard and S. J. Miklavcic, "Effective spring constant of bubbles and droplets," *Langmuir* **17**, 8217 (2001).
- ⁴⁰E. Klaseboer, J. P. Chevaillier, A. Maté, O. Masbernat, and C. Gourdon, "Model and experiments of a drop impinging on an immersed wall," *Phys. Fluids* **13**, 45 (2001).